(2)

ARMY RESEARCH LABORATORY

Deformation Mechanisms in Tungsten Single Crystals in Ballistic Impact Experiments

W. J. Bruchey, Jr.
R. N. Herring
P. W. Kingman
E. J. Horwath

ARL-TR-133 May 1993

NOTICES

Destroy this report when it is no longer needed. DO NOT return it to the originator.

Additional copies of this report may be obtained from the National Technical Information Service, U.S. Department of Commerce, 5285 Port Royal Road, Springfield, VA 22161.

The findings of this report are not to be construed as an official Department of the Army position, unless so designated by other authorized documents.

The use of trade names or manufacturers' names in this report does not constitute indorsement of any commercial product.

REPORT DOCUMENTATION PAGE

Form Approved
OMB No 0704-0188

1. AGENCY USE ONLY (Leave blank)	2. REPORT DATE	3. REPORT TYPE AND DATES COVERED
	May 1993	Final, 1 Oct 91 - 30 Sep 92

4. TITLE AND SUBTITLE

Deformation Mechanisms in Tungsten Single Crystals in Ballistic Impact Experiments

5. FUNDING NUMBERS

PR: 1L162618AH80

6. AUTHOR(S)

W. J. Bruchey, Jr., R. N. Herring, P. W. Kingman, and E. J. Horwath

7. PERFORMING ORGANIZATION NAME(S) AND ADDRESS(ES)

U.S. Army Research Laboratory
ATTN: AMSRL-WT-TA
Aberdeen Proving Ground, MD 21005-5066

8. PERFORMING ORGANIZATION REPORT NUMBER

9. SPONSORING/MONITORING AGENCY NAME(S) AND ADDRESS(ES)

U.S. Army Research Laboratory
ATTN: AMSRL-OP-CI-B (Tech Lib)
Aberdeen Proving Ground, MD 21005-5066

10. SPONSORING/MONITORING AGENCY REPORT NUMBER

ARL-TR-133

11. SUPPLEMENTARY NOTES

12a. DISTRIBUTION/AVAILABILITY STATEMENT

Approved for public release; distribution is unlimited.

12b. DISTRIBUTION CODE

13. ABSTRACT *(Maximum 200 words)*

The performance of tungsten single crystals in ballistic impact varies stongly as a function of crystallographic orientation. The deformation structure of recovered single crystal rods fired in ballistic environments has been characterized by optical microscopy, SEM and TEM, and x-ray diffraction. The observed microstructures are varied and provide substantial insights into the factors governing the penetration and flow behavior under ballistic conditions. Crystallographic orientation influences the potential for developing shear which enhances material flow, and this enhancement ultimately maximizes the energy available for target penetration. Microstructural analysis elucidates the various mechanisms occuring during the flow process for single crystals of high-symmetry orientations, and suggests possible analogies between the penetration behavior of the tungsten single crystals and other materials.

14. SUBJECT TERMS	15. NUMBER OF PAGES
crystallography; strain rate; dislocations; mass transfer; shear stresses	27
	16. PRICE CODE

17. SECURITY CLASSIFICATION OF REPORT	18. SECURITY CLASSIFICATION OF THIS PAGE	19. SECURITY CLASSIFICATION OF ABSTRACT	20. LIMITATION OF ABSTRACT
UNCLASSIFIED	UNCLASSIFIED	UNCLASSIFIED	UL

INTENTIONALLY LEFT BLANK.

TABLE OF CONTENTS

		Page
	LIST OF FIGURES	v
	ACKNOWLEDGMENT	vii
1.	INTRODUCTION	1
2.	MICROSTRUCTURAL INVESTIGATION - OPTICAL MICROSCOPY AND X-RAY DIFFRACTION	2
3.	TRANSMISSION MICROSCOPY	4
4.	CONCLUSIONS	12
5.	REFERENCES	17
	DISTRIBUTION LIST	19

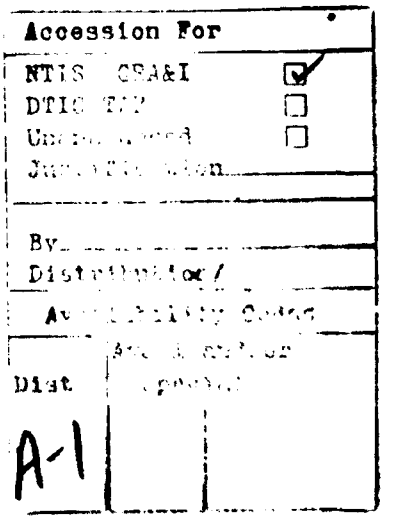

INTENTIONALLY LEFT BLANK.

LIST OF FIGURES

Figure		Page
1.	Optical Micrograph of Wavy Bifurcated Shear Bands in [110] Penetrator	3
2.	Optical Micrograph of Flow Pattern in [111] Penetrator Showing Unrecrystallized Material Surrounded by Shear Bands	5
3.	Optical Micrograph of [111] Penetrator Showing Shear Band Extending Into Residual Rod	5
4.	Crack Pattern in [100] Residual Penetrator	6
5.	Microstructure of [100] Penetrator Network of Fine Cracks in the Back Extruded Region	6
6.	Dislocation Arrangement in [100] Penetrator Showing: (a) Initial Stage of Subgrain Formation, (b) Formation of Well-Defined Grains and (c) Formation of Elongated Grains	8
7.	Recrystallized Region Showing Well-Defined Grains With Few or No Dislocations Within the Grains	9
8.	Dislocation Network in Regions Close to That Shown in Figure 6	9
9.	TEM Micrograph of [111] Penetrator Near the Outer Circumference	11
10.	TEM Micrograph of [111] Penetrator Showing the Dislocations as Either Pure Screws of Mixed Dislocations Containing Large Components	11
11.	General Microstructure of Deformed [110] Penetrator Showing (a) Heavily Dislocated Grains and (b) Some Recrystallization Which Has Produced Small Grains of Low Dislocation Density	12
12.	Dislocation Network in the [110] Penetrator Showing Two Beam Diffraction Conditions Which Put the Dislocation Groups Labelled A, B, C, In or Out of Contrast	13

INTENTIONALLY LEFT BLANK.

ACKNOWLEDGMENT

The authors would like to acknowledge the assistance of Mr. David MacKenzie, Terminal Effects Division, U.S. Army Research Laboratory, in sample preparation, microphotography, and timely preparation of target blocks for sectioning.

INTENTIONALLY LEFT BLANK.

1. INTRODUCTION

The material processes involved during the penetration of a long rod into a target block are not well understood. In a previous paper (Bruchey, Horwath, and Kingman 1991) presented at the 120th TMS Annual Meeting in February 1991, the ballistic results obtained from experiments using tungsten single crystal penetrators of high symmetry orientations fired into finite and semi-infinite steel target blocks were presented along with some preliminary metallographic observations of the residual penetrators. More detailed analysis is now available and will be discussed in this report.

Large-caliber penetrators used in modern day tank gun ammunition rely on the penetration performance of high-density alloys. These efforts have historically centered on the uranium and tungsten containing alloys. The uranium research has dealt with evaluations of most of the binary alloys such as U-0.75Ti and U-2Mo. Tungsten research has centered on the W-Ni-Fe alloys/composites. Both categories of materials have densities greater than 17.

In recent years, there has been considerable interest in developing tungsten materials which could be used as a substitute for uranium materials. As a precursor to tungsten alloy development, a better understanding of how the constituents of these alloys/composites behave under ballistic impact condition is required. To address this issue, a small (geometrical) scale program was initiated to assess the flow and failure behavior of single crystal tungsten rods against various target geometries. As previously reported, the single crystals of tungsten in three orientations, [111], [110], and [100], were obtained commercially and were grown using the Czochralski (CZ) technique after preliminary two pass zone refinement of 99.99% purity starting material.

The ballistic experiments have been described in detail previously. Only the principal results pertinent to the following discussion will be summarized here. Model long rod penetrators of 6.90 mm diameter and 102.5 mm length were prepared from tungsten single crystals of high symmetry orientations ([100], [111], and [110]) and fired into steel target blocks at a velocity of 1,500 m/s. In each case, the crystal axis was aligned parallel to the rod axis. A summary of the average penetration results for each of the penetrators fired into semi-infinite steel blocks is listed in Table 1. The penetration performance was found to vary

Table 1. Penetration Test Summary for Rods Fired Into Semi-Infinite Blocks of RHA Steel

MATERIAL	PENETRATION/UNIT ROD LENGTH P/L
93W-Ni-Fe Ordnance Alloy	0.84
U-0.75Ti Ordnance Alloy	0.95
[111] W Single Crystal	0.88
[110] W Single Crystal	0.83
[100] W Single Crystal	0.97

with orientation, with [100] providing the best penetration and [110] the poorest. Of particular interest, the [100] orientation outperformed a comparison 93-WHA rod in the same test and matched the performance of the U-0.75Ti grade ordnance alloy. An extended description of the ballistic tests and data analysis is contained in the previous reference. Initial macroscopic examination of polished sections of the rod embedded in the semi-infinite target blocks showed that all of the single crystal penetrators had deformed by eversion. The material at the front of the penetrator back-extruded to form a continuous hollow tube extending back along the cavity from the small residual slug at the end of the cavity. The exterior surface of the hollow tube was essentially continuous, but the interior (concave) surface was covered with a regular pattern of exfoliation. The detailed flow pattern for each orientation was quite different and the effect of orientation was observed not only in the region immediately surrounding the nose of the residual penetrator, but in the foliation pattern within the extruded tube as well. Apparent differences in the amount of shear localization as a function of orientation were concluded to be a major factor in the partition of energy during penetration and flow. However, it was apparent that further investigation of the microstructure was necessary to further elucidate the material processes.

2. MICROSTRUCTURAL INVESTIGATION - OPTICAL MICROSCOPY AND X-RAY DIFFRACTION

The previously sectioned crystals embedded in the semi-infinite target blocks were subsequently etched and examined metallographically. The sections were also x-rayed using

a standard back-reflection technique in order to determine the crystal orientation and a general indication of lattice distortion, polygonization, and recrystallization. Portions of the samples were then sectioned and thinned for transmission electron microscopy to determine the dislocation structure. In addition, a limited amount of scanning electron microscopy was performed on segments of the back-extruded material which separated from the main specimen.

The [110] penetrator, which achieved the poorest penetration, flowed in a very inhomogeneous and asymmetric manner with extensive lattice rotation. Figure 1 shows the wavy, bifurcated deformation bands typically observed in the flowed region. The remnant residual rod cracked and fractured into large fragments rotated with respect to one another. X-ray patterns in the flowed portion indicate extensive recrystallization. In some regions, strong deformation textures occur, while in others, sharp reflections from freshly recrystallized grains are observed.

Figure 1. Optical Micrograph of Wavy Bifurcated Shear Bands in [110] Penetrator.

The flowed material from the [111] penetrator also contained deformation bands, often with small regions of parent single crystal material entrained between the bands (Figure 2). Unlike the [110], a distinct rod remnant approximately equal in length to the rod diameter remained. The only visible deformation features within this residual rod are several narrow bands running from the edge of the rod into the interior (Figure 3). Separation of material from the end of the rod was probably initiated by the formation of these shear zones.

The microstructure of the [100] penetrator is quite different from the shear band pattern seen in the other orientations. Etching of the polished surface delineated an extended pattern of fine cracks with a separation on the order of 0.1 mm extending throughout the sample (Figure 4). Superimposed on this is a more irregular pattern of cracks and fractures on a larger scale. Both of these crack and fracture patterns extend throughout the residual rod and into the back extrusion region as well (Figure 5). Only in limited areas are deformation bands observed, and the single crystal character is largely maintained through the initial flow until recrystallization occurs in the back extrusion region.

3. TRANSMISSION MICROSCOPY

Specimens were prepared for transmission microscopy by standard techniques. After cutting thin wafers from the bulk material by slow-speed diamond cutting, discs were spark machined and then hand ground to 50–100 μm. Final thinning was done with 2% NaOH solution at 40 V using a jet polisher. A major problem was the tendency of the samples to breakup due to cracks, inhomogeneities, etc., which occurred during the final stages of preparation. Both longitudinal and transverse sections were made, but the efforts to produce transverse samples met with more limited success.

Microscopy was done with a Phillips EM 300 at 100 kV and a Phillips EM 430 at 300 kV. Burgers vectors, line directions, and habit planes of the observed dislocation arrays were characterized by systematic contrast experiments under many different two-beam diffraction conditions. The Burgers vectors were determined from the $g.b = 0$ condition, as well as by the contrast shown by the dislocations when $g.b = 1, 2$, or more. Although the general location from which the discs were taken was documented, due to time constraints, it was not feasible to maintain unique reference coordinates during specimen preparation. Thus, the

Figure 4. Crack Pattern in [100] Residual Penetrator.

Figure 5. Microstructure of [100] Penetrator Network of Fine Cracks in the Back Extruded Region.

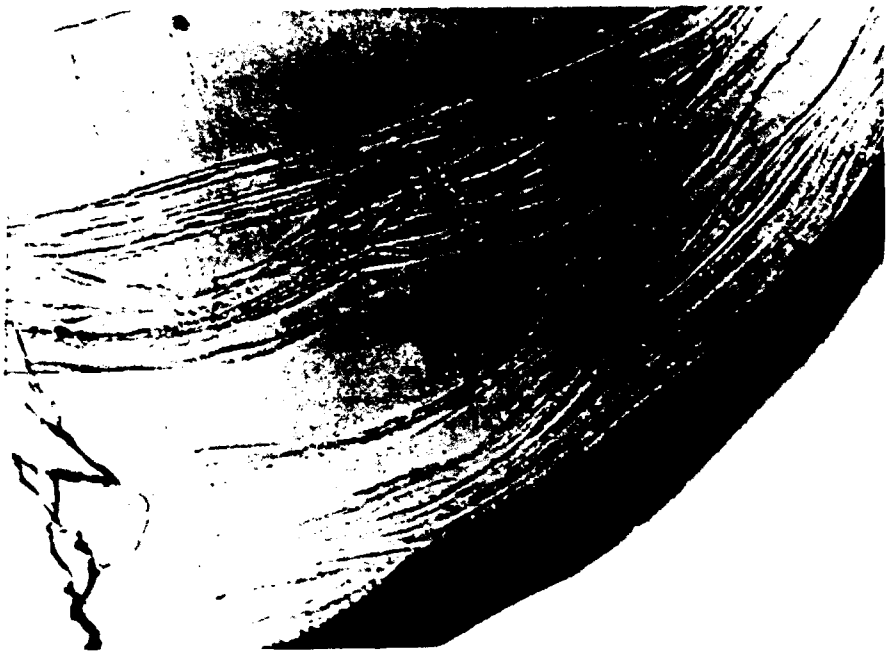

Figure 2. Optical Micrograph of Flow Pattern in [111] Penetrator Showing Unrecrystallized Material Surrounded by Shear Bands.

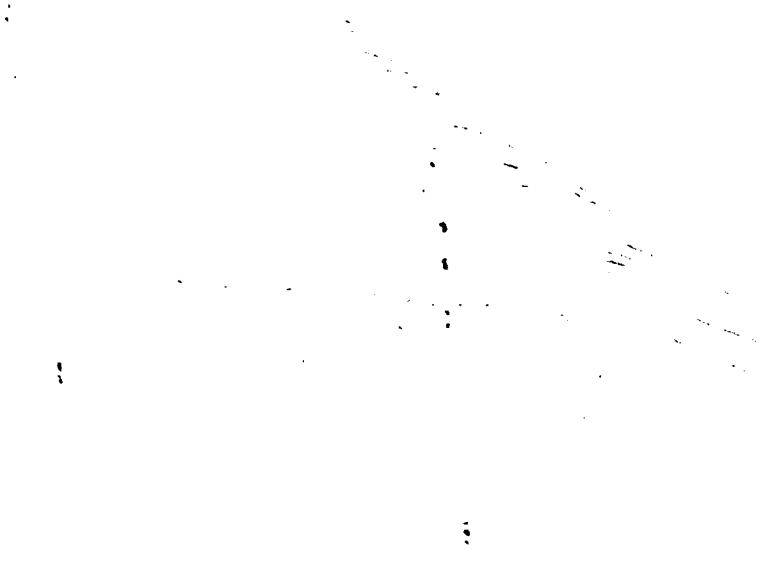

Figure 3. Optical Micrograph of [111] Penetrator Showing Shear Band Extending Into Residual Rod.

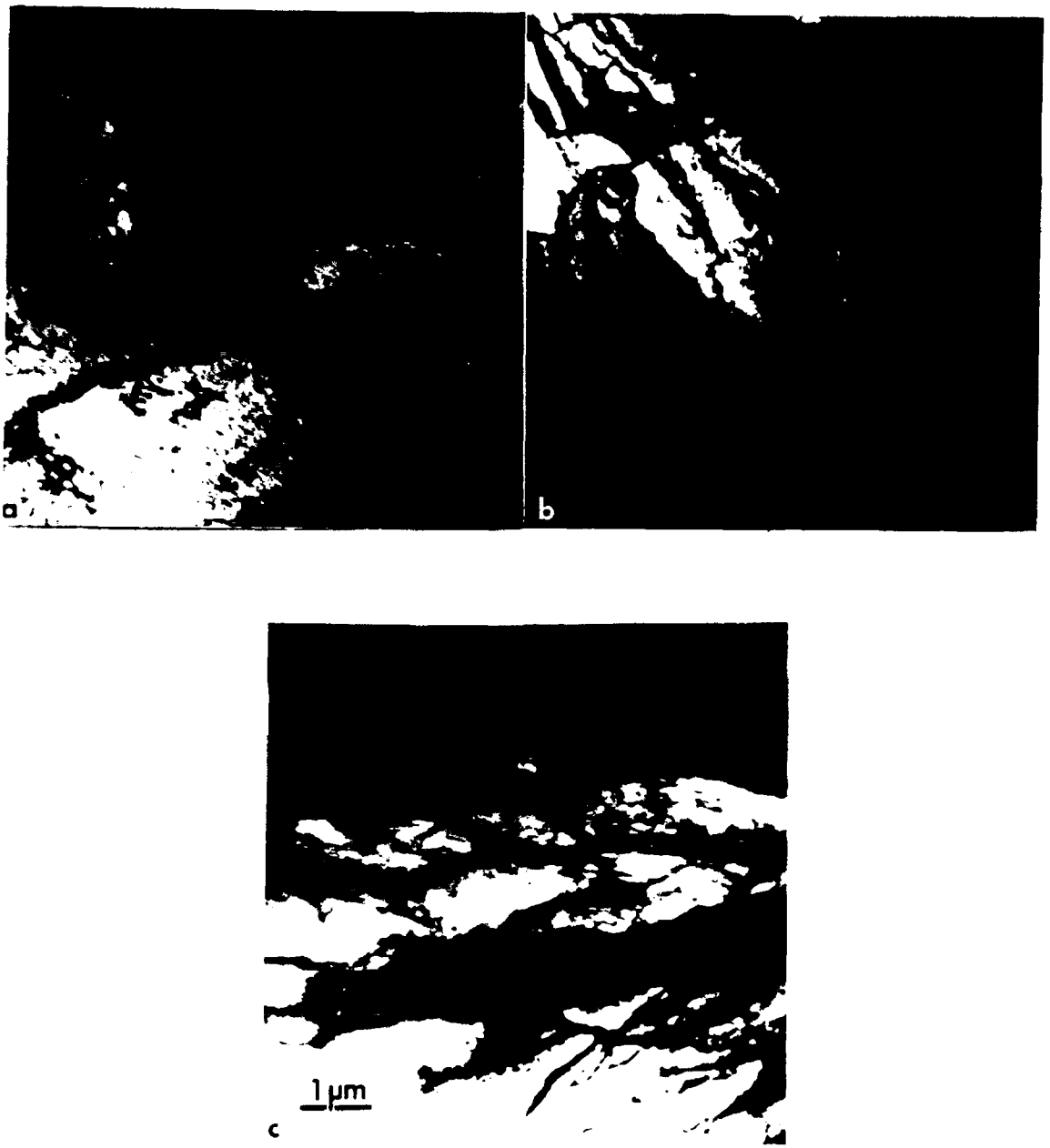

Figure 6. Dislocation Arrangement in [100] Penetrator Showing: (a) Initial Stage of Subgrain Formation, (b) Formation of Well-Defined Grains and (c) Formation of Elongated Grains.

crystallographic directions assigned during the analysis are arbitrary and cannot be correlated with the original penetrator or stress axes.

• TEM Results. A wide variety of microstructures was observed. This is to be expected from the inhomogeneity of the deformation process previously noted, and also from the general flow pattern in which severely worked material extrudes back adjacent to the remaining undeformed penetrator. However, certain microstructural patterns were generally observed. Dislocations were found with Burgers vectors of 1/2<111>. No other type of defect which could produce deformation was found. The dislocations polygonized the crystal by forming grain boundaries. Recrystallization of the grains removed the dense dislocation networks and was seen in material a few hundreds of micrometers from regions which appeared to have been freshly deformed. This process is illustrated in the sequence of micrographs in Figures 6a, 6b, and 6c from a region near the penetrator/target interface of the [100] penetrator. In Figure 6a, the dislocations form dense arrays which are the basis for subgrain formation. Well-defined grain boundaries have begun to form in Figure 6b and, in Figure 6c, elongated grains have formed with a high density of dislocations within themselves. Figure 7 shows a recrystallized region from the [111] penetrator with well-defined grains of different orientation and few interior dislocations. Similar general microstructure occurred in all penetrators, but the dislocation networks at subgrain boundaries were significantly different for each orientation, which was indicative of their different dislocation generation mechanisms. Examples for each orientation follow.

The dislocation network from a region of the [100] penetrator close to that of Figure 6 is shown in Figure 8. Four sets of dislocations labelled A–D dominate the microstructure. Detailed contrast analysis showed these dislocations to have four distinct Burgers vectors of the type 1/2<111> and to be either pure screws or mixed dislocations with a large screw component. The habit planes of the dislocations were either {110} or {112}.

The general appearance of a longitudinal specimen taken from the [111] penetrator near the outer circumference is shown in Figure 9. Subgrain boundaries containing a dense, orderly array of dislocations have formed. An adjacent region containing a dislocation network shown in Figures 10a, 10b, and 10c was analyzed in detail. The dislocation types A, B, and C have three distinct Burgers vectors of type 1/2 <111>. Figure 10a shows the complete

Figure 7. Recrystallized Region Showing Well-Defined Grains With Few or No Dislocations Within the Grains.

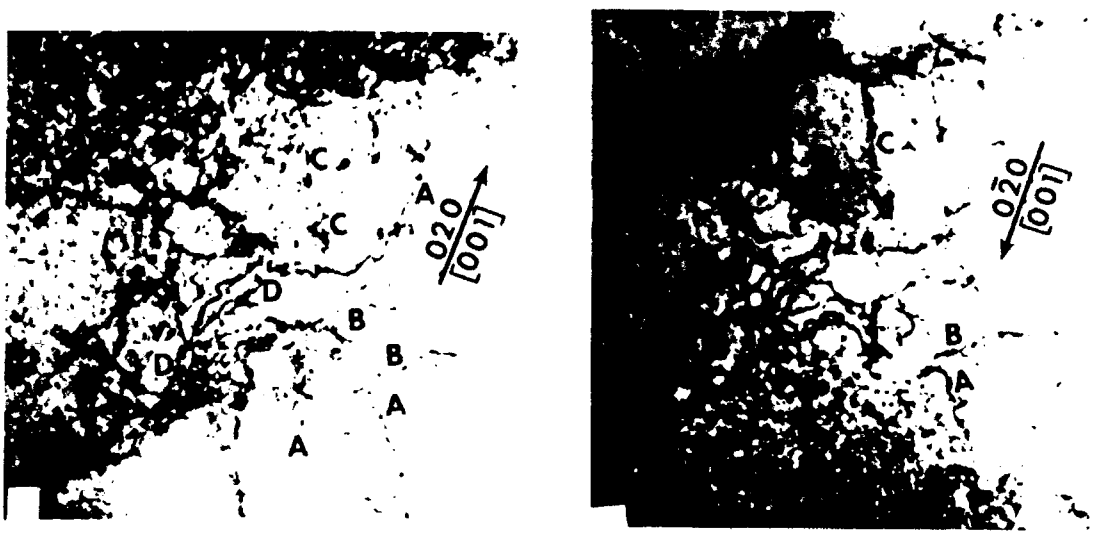

Figure 8. Dislocation Network in Regions Close to That Shown in Figure 6.

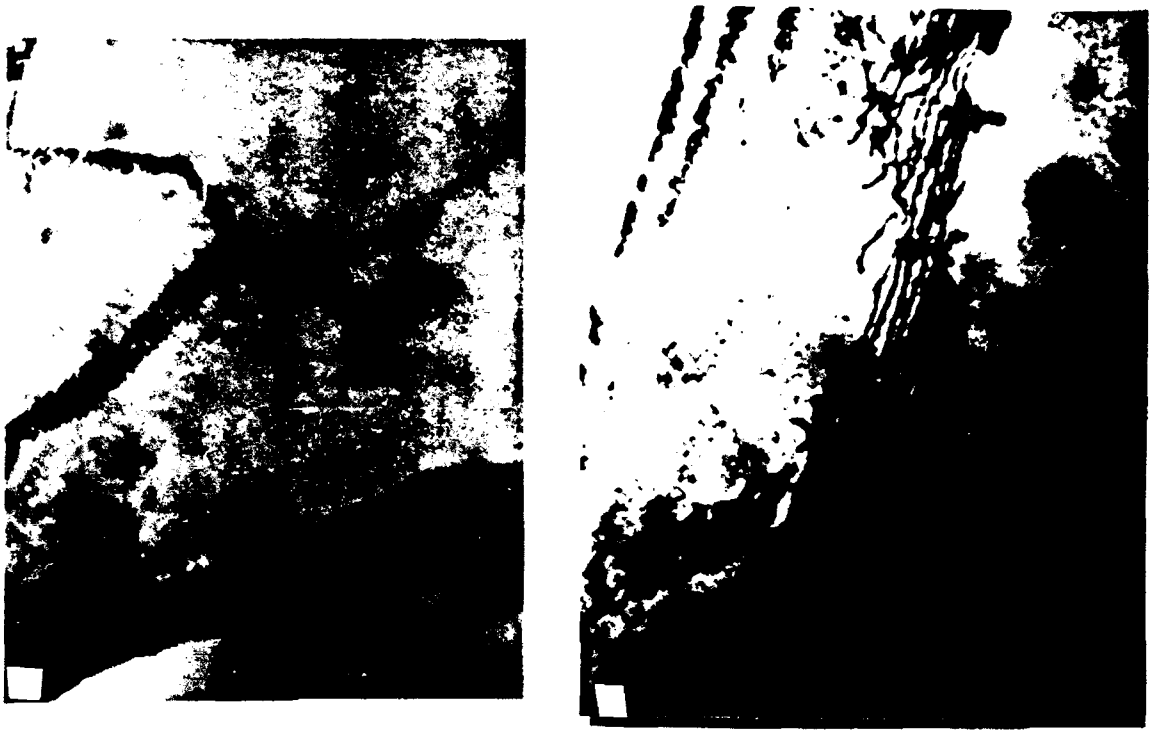

Figure 9. TEM Micrograph of [111] Penetrator Near the Outer Circumference.

Figure 10. TEM Micrograph of [111] Penetrator Showing the Dislocations as Either Pure Screws of Mixed Dislocations Containing Large Components.

network, while Figures 10b and 10c show A and B, respectively, out of contrast. Analysis of the line directions and habit planes shows that A and B are either pure screws or mixed dislocations containing large screw components.

The morphology of dislocation arrays in the [110] penetrator is shown in Figures 11a (elongated grains with a high density of dislocations) and 11b (small, also recrystallized grains of low dislocation density). An adjacent region was analyzed for dislocations, as shown in Figures 12a, 12b, and 12c. Three similar types of dislocations labelled A, B, and C dominate the microstructure. Analysis showed that each of these has a unique Burgers vector of type 1/2<111>, and that the long, straight dislocations of types A and B are pure screws having Burgers vectors (and line directions) $[11\bar{1}]$ and $[1\bar{1}1]$, respectively. Upon closer examination, both of these dislocation types are seen to contain short segments which are perpendicular to the principal line direction, as seen in Figure 12b for diffraction condition $0\bar{1}1$g [311]. The arrowed segments of the dislocations A disappear for diffracting condition $(\bar{1}01)$g[131] (Figure 12c) and, thus, have u~[131], which is also close to [211]. Thus, they are pure edge dislocations lying on (211) or $(1\bar{1}0)$ slip planes. Similarly, the arrowed segments of dislocations B disappear for $(\bar{2}1\bar{1})$g[001] (Figure 12d) and, thus, have u~[311], making them pure edge dislocations lying on $(21\bar{1})$ which is not far from the $(2\bar{1}1)$ and $(1\bar{1}0)$ slip planes of the dislocations A. The habit planes for the C dislocations were not determined since the line directions were difficult to follow.

To summarize, in all three orientations, dislocations of type 1/2 <111> were found, and no defects such as twins or stacking faults were observed. However, the dislocation networks varied as a function of orientation. For the [100] orientation, the arrays tended to be tangled and disorderly, as would be produced by the motion of screw dislocations or mixed dislocations with a large screw component. For the [110] orientation, an extensive and moderately orderly array containing many long, straight pure screw dislocations with edge segments at the ends occurred. This type of structure is typical of that left by pure edge dislocations passing through the crystal. The networks in the [111] crystal were quite orderly, but the dislocations tended to be wavy or bowed, like those seen in the [100]. Such dislocations tend to be produced by the motion of screws or mixed dislocations with strong screw character.

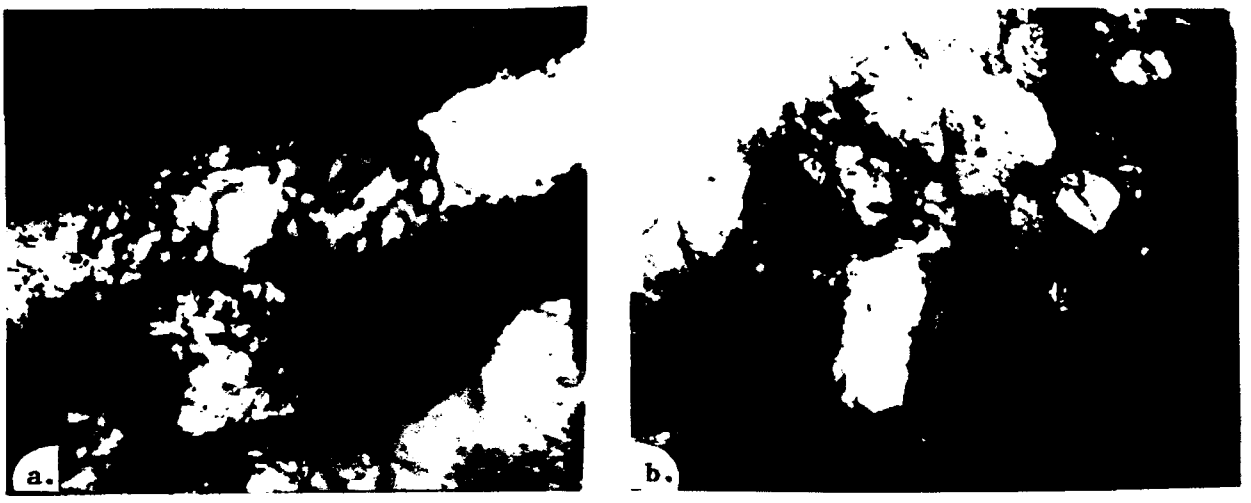

Figure 11. General Microstructure of Deformed [110] Penetrator Showing (a) Heavily Dislocated Grains and (b) Some Recrystallization Which Has Produced Small Grains of Low Dislocation Density.

4. CONCLUSIONS

The combined results described above provide additional insight into the material flow processes occurring during penetration. Although a significant amount of research has been performed on the deformation of tungsten single crystals, there is still no coherent description of the deformation mechanisms or work-hardening behavior. The present study clearly shows that deformation proceeds by the generation and interaction of dislocations of Burgers vector 1/2 <111> to form dislocation networks, subboundaries, and eventually recrystallization. No other defects such as twins or stacking faults were observed.

Crystallographic symmetry governs the operative dislocation systems in the initiation of deformation, and this establishes the eventual continuing course of deformation. The dislocation networks for the [100] penetrator were tangled arrays of bowed or wavy dislocations, while the dislocations in the [111] were similar, but the arrays were more orderly.

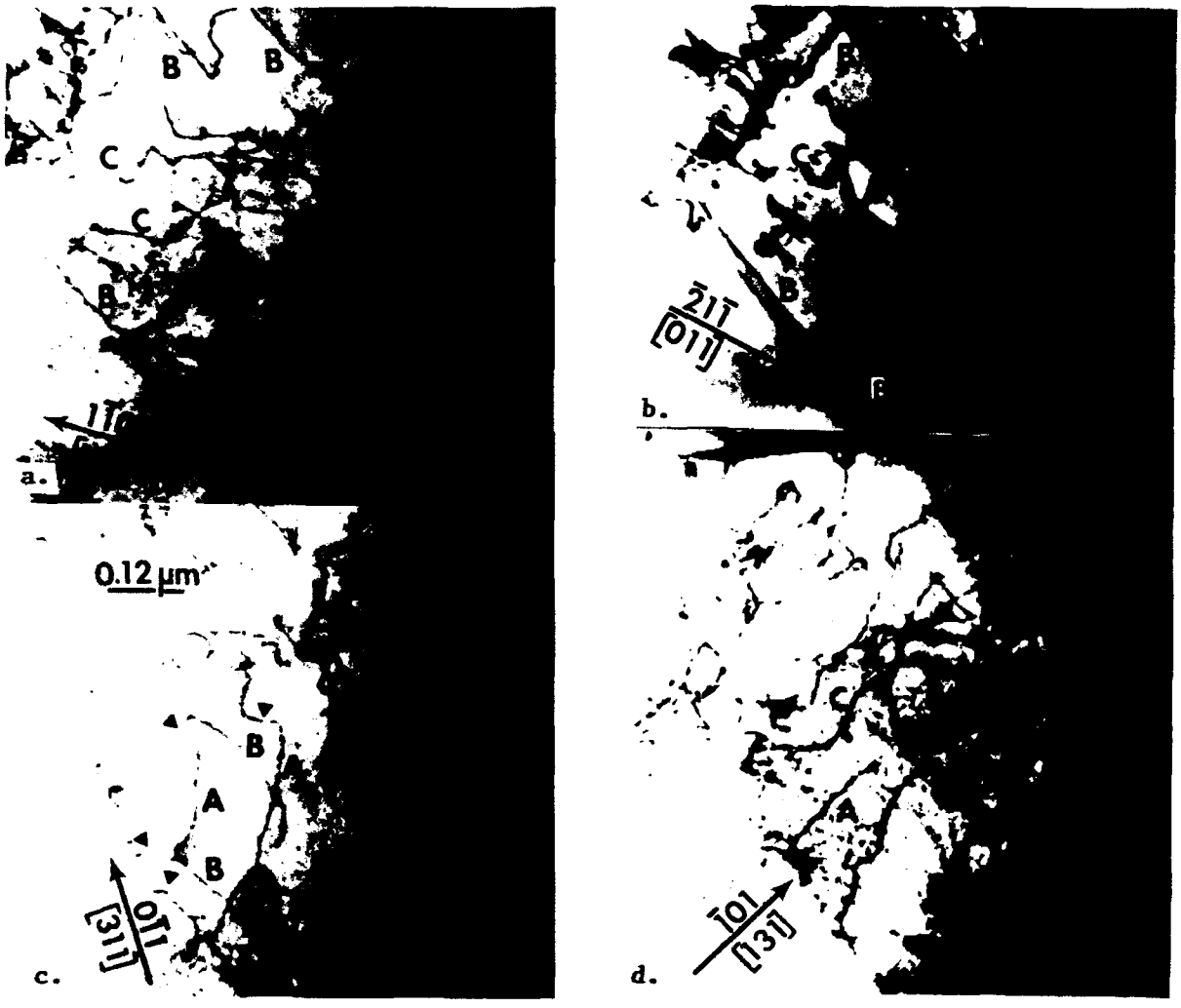

Figure 12. Dislocation Network in the [110] Penetrator Showing Two Beam Diffraction Conditions Which Put the Dislocation Groups Labelled A, B, C In or Out of Contrast.

In the [110] penetrator, straight screw dislocations with edge segments at the ends were found, implying that they were left behind by edge dislocations.

For the [100] (four-fold) axis, four <111> vectors lie at 54.7° from the stress axis. In addition, there are multiple {110} and also {112} planes which are favorably oriented for resolved shear stress, and the dislocations lying in these planes have a large screw component. This provides ample opportunity for dislocation motion and interaction, leading to the dense, wavy dislocation arrays observed here. This is in agreement with the work-hardening that was observed for this orientation previously (Beardmore and Hull 1965; Argon and Maloof 1966; Rose, Ferriss, and Wulf 1962).

In the [111] (3-fold) orientation, the three available <111> vectors are 70.5° from the stress axis. This results in resolved shear stresses on the slip systems that are relatively low. However, when the stresses become sufficient to initiate dislocation motion and interaction, orderly arrays are formed.

At the [110] (2-fold) axis, two <111> vectors lie in the plane normal to the stress axis, while the two operative <111> vectors are only 35° from the stress axis, and thus have a high resolved shear stress. It is apparent from the TEM analysis that slip by pure edge dislocations is operative. The overall behavior is highly asymmetric and in agreement with observations by other investigators (Argon and Maloof 1966; Rose, Ferris, and Wulf 1962).

Extensive cracking was observed macroscopically in the [100] penetrator. The reaction

$$a/2[111] + a/2[1\bar{1}\bar{1}] \Rightarrow a\,[100]$$

was suggested by Cottrell as a potential source for the initiation of cleavage cracks on {100}. Cleavage fractures on {100}, particularly in <100> oriented crystals, have been observed in bcc materials, including tungsten (Beardmore and Hull 1965).

As the material flows around the penetrator, it experiences intense working and increased temperature. As penetration occurs, the material experiences high stresses and temperature increases. When the material flows at high strains, a progressive process of recrystallization

and deformation undoubtedly occurs, leading to a highly textured substructure. This continuous process would also lead to the final microstructure where newly recrystallized, dislocation-free grains exist adjacent to regions which have freshly deformed.

Recrystallization of the grains removed the dense dislocation networks and was seen in close proximity to regions which appeared to have freshly deformed. The regions which are deforming at or near the penetrator/RHA interface are at relatively high temperature and there is sufficient energy to undergo recrystallization. It is likely that recrystallization of a given piece of material occurs a number of times during its course of flow from the head of the penetrator to the side wall of the cavity.

The general deformation mechanism and mass transfer from the penetrator to the walls of the cavity can be summarized as follows. The dislocations polygonized the single crystal by forming grain boundaries. The dislocations thread their way through the crystal and form dense arrays or subgrain boundaries and, eventually, they form elongated grains with a high density of dislocations within the grains. The flow of dislocations along these subgrain and grain boundaries produces a mass transfer in a direction within the plane of the boundary. Mass transfer along the subgrain boundaries reorients the grains to form well-defined grains and boundaries. Further mass transfer along the grain boundaries results in the grains becoming elongated in the direction of mass flow, similar to that of rolled or forged material.

The [100] and [111] oriented penetrators both produce deep penetration into RHA with the [100] orientation penetrating deepest. Both directions have symmetric multiple deformation systems which provide an even mass transfer to the wall of the cavity. The difference lies in the [100] producing dislocations on slip planes and the [111] producing pure screw dislocations which do not have a slip or glide plane. The [110] penetrator has only two-fold symmetry. This results in a less symmetric (elliptical) deformation cross section and also fewer available slip systems and lower work-hardening during flow. As a result, penetration depth is decreased.

In summary, it has been shown that crystal properties can have a significant effect on material behavior at the very high strain rates experienced during ballistic impact and penetration. While single crystals may not be generally employed as long rod penetrators,

this study suggests that crystal structure and texture could play a significant role in material performance and should be given consideration in the search for improved performance materials.

5. REFERENCES

Argon, A., and S. Maloof. "Plastic Deformation of Tungsten Single Crystals at Low Temperature." Acta Metallurgica, vol. 14, p. 1449, 1966.

Beardmore, P., and D. Hull. "Deformation and Fracture of Tungsten Single Crystals." Journal of Less-Common Metals, vol. 9, p. 168, 1965.

Bruchey, W. J., E. J. Horwath, and P. W. Kingman. "Orientation Dependence of Deformation and Penetration Behavior of Tungsten Single Crystal Rods." Tungsten and Tungsten Alloys: Recent Advances, A. Crowson, E. S. Chen, Eds. The Minerals, Metals, and Materials Society, Warrendale, PA, pp. 121–128, 1991.

Rose, R., D. Ferriss, and J. Wulf. "Yielding and Plastic Flow in Single Crystals of Tungsten." Trans. Metallurgical Society AIME, vol. 224, p. 981, 1962.

INTENTIONALLY LEFT BLANK.

No. of Copies	Organization
2	Administrator Defense Technical Info Center ATTN: DTIC-DDA Cameron Station Alexandria, VA 22304-6145
1	Commander U.S. Army Materiel Command ATTN: AMCAM 5001 Eisenhower Ave. Alexandria, VA 22333-0001
1	Director U.S. Army Research Laboratory ATTN: AMSRL-OP-CI-AD, Tech Publishing 2800 Powder Mill Rd. Adelphi, MD 20783-1145
1	Director U.S. Army Research Laboratory ATTN: AMSRL-OP-CI-AD, Records Management 2800 Powder Mill Rd. Adelphi, MD 20783-1145
2	Commander U.S. Army Armament Research, Development, and Engineering Center ATTN: SMCAR-IMI-I Picatinny Arsenal, NJ 07806-5000
2	Commander U.S. Army Armament Research, Development, and Engineering Center ATTN: SMCAR-TDC Picatinny Arsenal, NJ 07806-5000
1	Director Benet Weapons Laboratory U.S. Army Armament Research, Development, and Engineering Center ATTN: SMCAR-CCB-TL Watervliet, NY 12189-4050
(Unclass. only)1	Commander U.S. Army Rock Island Arsenal ATTN: SMCRI-IMC-RT/Technical Library Rock Island, IL 61299-5000
1	Director U.S. Army Aviation Research and Technology Activity ATTN: SAVRT-R (Library) M/S 219-3 Ames Research Center Moffett Field, CA 94035-1000

No. of Copies	Organization
1	Commander U.S. Army Missile Command ATTN: AMSMI-RD-CS-R (DOC) Redstone Arsenal, AL 35898-5010
1	Commander U.S. Army Tank-Automotive Command ATTN: ASQNC-TAC-DIT (Technical Information Center) Warren, MI 48397-5000
1	Director U.S. Army TRADOC Analysis Command ATTN: ATRC-WSR White Sands Missile Range, NM 88002-5502
1	Commandant U.S. Army Field Artillery School ATTN: ATSF-CSI Ft. Sill, OK 73503-5000
(Class. only)1	Commandant U.S. Army Infantry School ATTN: ATSH-CD (Security Mgr.) Fort Benning, GA 31905-5660
(Unclass. only)1	Commandant U.S. Army Infantry School ATTN: ATSH-CD-CSO-OR Fort Benning, GA 31905-5660
1	WL/MNOI Eglin AFB, FL 32542-5000
	Aberdeen Proving Ground
2	Dir, USAMSAA ATTN: AMXSY-D AMXSY-MP, H. Cohen
1	Cdr, USATECOM ATTN: AMSTE-TC
1	Dir, ERDEC ATTN: SCBRD-RT
1	Cdr, CBDA ATTN: AMSCB-CI
1	Dir, USARL ATTN: AMSRL-SL-I
10	Dir, USARL ATTN: AMSRL-OP-CI-B (Tech Lib)

No. of Copies Organization

1 Director
U.S. Army Research Office
ATTN: A. Crowson
P.O. Box 12211
Research Triangle Park, NC
27709-2211

1 Director
U.S. Army Research Office
ATTN: I. Iyer
P.O. Box 12211
Research Triangle Park, NC
27709-2211

1 Director
U.S. Army Research Office
ATTN: J. Wu
P.O. Box 12211
Research Triangle Park, NC
27709-2211

3 Director
U.S. Army Research Laboratory
Materials Directorate
ATTN: AMSRL-MA,
S. Chou
J. Dandekar
Watertown, MA 02172-0001

1 Commander
U.S. Army Tank-Automotive Research
and Development Center
ATTN: AMSTA-RSS
Warren, MI 48397-5000

1 U.S. Naval Academy
Department of Mathematics
ATTN: R. Malek-Madani
Annapolis, MD 21402

1 Air Force Armament Laboratory
ATTN: J. Foster
Eglin AFB, FL 32542-5438

1 Air Force Wright Aeronautical Laboratories
Air Force Systems Command Materials
Laboratory
ATTN: T. Nicholas
Wright-Patterson AFB, OH 45433

No. of Copies Organization

3 Director
Sandia National Laboratories
ATTN: L. Davison
W. Herrmann
P. Chen
P.O. Box 5800
Albuquerque, NM 87285-5800

1 Director
Sandia National Laboratories
ATTN: S. Passman
P.O. Box 5800
Albuquerque, NM 87285-5800

1 Director
Sandia National Laboratories
ATTN: M. Forrestal
P.O. Box 5800
Albuquerque, NM 87285-5800

1 Director
Sandia National Laboratories
ATTN: D. Bammann
Livermore, CA 94550

1 National Institute of Science
and Technology
ATTN: T. Burns
Technology Building, Room A151
Gaithersburg, MD 20899

1 University of Missouri-Rolla
Dept. of Mechanical and
Aerospace Engineering
ATTN: R. Batra
Rolla, MO 65401-0249

1 California Institute of Technology
Division of Engineering and
Applied Science
ATTN: J. Knowles
Pasadena, CA 91102

1 Massachusetts Institute of Technology
Dept. of Mechanical Engineering
ATTN: L. Anand
Cambridge, MA 02139

No. of Copies Organization

2 Rennselaer Polytechnic Institute
Department of Mechanical Engineering
ATTN: E. Lee
E. Krempl
Troy, NY 12181

1 Rennselaer Polytechnic Institute
Dept. of Computer Science
ATTN: J. Flaherty
Troy, NY 12181

1 Brown University
Division of Engineering
ATTN: R. Clifton
Providence, RI 02912

1 Brown University
Division of Engineering
ATTN: B. Freund
Providence, RI 02912

1 Brown University
Division of Engineering
ATTN:A Needleman
Providence, RI 02912

1 Brown University
Division of Applied Mathematics
ATTN: C. Dafermos
Providence, RI 02912

1 Carnegie-Mellon University
Dept. of Mathematics
ATTN: D. Owen
Pittsburg, PA 15213

1 Carnegie-Mellon University
Dept. of Mathematics
ATTN: M. Gurtin
Pittsburg, PA 15213

1 Cornell University
Dept. of Theoretical and Applied Mechanics
ATTN: J. Jenkins
Ithaca, NY 14850

1 Cornell University
Dept. of Theoretical and Applied Mechanics
ATTN: P. Rosakis
Ithaca, NY 14850

No. of Copies Organization

1 Cornell University
Dept. of Theoretical and Applied Mechanics
ATTN: W. Sachse
Ithaca, NY 14850

1 Cornell University
Dept. of Theoretical and Applied Mechanics
ATTN: T. Healey
Ithaca, NY 14850

1 Cornell University
Dept. of Theoretical and Applied Mechanics
ATTN: A. Zehnder
Ithaca, NY 14850

1 Harvard University
Division of Engineering and Applied Physics
ATTN: J. Rice
Cambridge, MA 02138

1 Harvard University
Division of Engineering and Applied Physics
ATTN: J. Hutchinson
Cambridge, MA 02138

1 North Carolina State University
Dept. of Civil Engineering
ATTN: Y. Horie
Raleigh, NC 27607

1 Rice University
Dept of Mathematical Sciences
ATTN: C. C. Wang
P.O. Box 1892
Houston, TX 77001

1 The Johns Hopkins University
Dept. of Mechanical Engineering
Latrobe Hall
ATTN: W. Sharp
34th and Charles Streets
Baltimore, MD 21218

1 The Johns Hopkins University
Dept. of Mechanical Engineering
Latrobe Hall
ATTN: G. Bao
34th and Charles Streets
Baltimore, MD 21218

No. of Copies Organization

1 The Johns Hopkins University
Dept. of Mechanical Engineering
Latrobe Hall
ATTN: K. T. Ramesh
34th and Charles Streets
Baltimore, MD 21218

1 The Johns Hopkins University
Dept. of Mechanical Engineering
Latrobe Hall
ATTN: A. Douglas
34th and Charles Streets
Baltimore, MD 21218

1 University of California
at Santa Barbara
Dept of Materials Science
ATTN: A. Evans
Santa Barbara, CA 93106

1 University of California
at San Diego
Dept. of Applied Mechanics and
Engineering Sciences
ATTN: S. Nemat-Nasser
La Jolla, CA 92093

1 University of California
at San Diego
Dept. of Applied Mechanics and
Engineering Sciences
ATTN: M. Meyers
La Jolla, CA 92093

1 University of California
at San Diego
Dept. of Applied Mechanics and
Engineering Sciences
ATTN: X. Markenscoff
La Jolla, CA 92093

1 University of California
at San Diego
Dept. of Applied Mechanics and
Engineering Sciences
ATTN: A. Hoger
La Jolla, CA 92093

No. of Copies Organization

1 University of California
at San Diego
Dept. of Applied Mechanics and
Engineering Sciences
ATTN: R. Asaro
La Jolla, CA 92093

1 Northwestern University
Dept. of Applied Mathematics
ATTN: W. Olmstead
Evanston, IL 60201

1 University of Florida
Dept. of Engineering Science and
Mechanics
ATTN: L. Malvern
Gainesville, FL 32601

1 University of Florida
Dept. of Engineering Science and
Mechanics
ATTN: D. Drucker
Gainesville, FL 32601

1 University of Florida
Dept. of Engineering Science and
Mechanics
ATTN: M. Eisenberg
Gainesville, FL 32601

1 University of Houston
Dept. of Mechanical Engineering
ATTN: L. Wheeler
Houston, TX 77004

1 University of Illinois
Dept. of Theoretical and
Applied Mechanics
ATTN: D. Carlson
Urbana, IL 61801

1 University of Illinois at
Chicago Circle
Dept. of Engineering, Mechanics,
and Metallurgy
ATTN: T. Ting
P.O. Box 4348
Chicago, IL 60680

No. of Copies | Organization

1 University of Kentucky
Dept. of Engineering Mechanics
ATTN: O. Dillon, Jr.
Lexington, KY 40506

1 University of Maryland
Dept. of Mathematics
ATTN: S. Antman
College Park, MD 20742

1 University of Maryland
Dept. of Mathematics
ATTN: T. Liu
College Park, MD 20742

1 University of Minnesota
Dept. of Aerospace Engineering and Mechanics
ATTN: R. Fosdick
110 Union Street SE
Minneapolis, MN 55455

1 University of Minnesota
Dept. of Aerospace Engineering and Mechanics
ATTN: R. James
110 Union Street SE
Minneapolis, MN 55455

1 University of Oklahoma
School of Aerospace, Mechanical and Nuclear Engineering
ATTN: C. Bert
Norman, OK 73019

1 University of Texas
Dept. of Engineering Mechanics
ATTN: J. Oden
Austin, TX 78712

1 University of Washington
Dept. of Aeronautics and Astronautics
ATTN: I. Fife
206 Guggenheim Hall
Seattle, WA 98195

No. of Copies | Organization

1 University of Maryland
Dept. of Mechanical Engineering
ATTN: R. Armstrong
College Park, MD 20742

1 University of Maryland
Dept. of Mechanical Engineering
ATTN: J. Dally
College Park, MD 20742

1 University of Wyoming
Dept. of Mathematics
ATTN: R. Ewing
P.O. Box 3036
University Station
Laramie, WY 82070

1 Washington State University
Mechanical and Materials Engineering
ATTN: H. M. Zbib
Pullman, WA 99164

1 Yale University
Dept. of Mechanical Engineering
ATTN: E. Onat
400 Temple Street
New Haven, CT 96520

1 Southwest Research Institute
Department of Mechanical Sciences
ATTN: U. Lindholm
8500 Culebra Road
San Antonio, TX 02912

1 Southwest Research Institute
Department of Mechanical Sciences
ATTN: C. Anderson
8500 Culebra Road
San Antonio, TX 02912

1 Southwest Research Institute
Department of Mechanical Sciences
ATTN: J. Lankford
8500 Culebra Road
San Antonio, TX 02912

No. of Copies | Organization

1 The Johns Hopkins University
Materials Science and Engineering
ATTN: R. E. Green
102 Maryland Hall
Baltimore, MD 21218

1 University of Nebraska
Engineering Mechanics
ATTN: M. Beatty
212 Bancroft Hall
Lincoln, NE 68588

1 Oklahoma State University
ATTN: R. M. Bowen
101 Whitehurst Hall
Stillwater, OK 74078

1 University of Maryland
Baltimore County
Mechanical Engineering
ATTN: A. Khan
Baltimore, MD 21228

1 University of Wisconsin
Dept. of Mathematics
ATTN: A. Tzavaras
Madison, WI 53706

1 California Institute of Technology
ATTN: G. Ravichandran
Mail Code 105-50
Pasadena, CA 91125

1 State University of New York
at Stony Brook
Applied Mathematics and Statistics
P138A Mathematics
ATTN: J. Glimm
Stony Brook, NY 11794

1 University of Virginia
Dept. of Applied Mathematics
ATTN: C. O. Horgan
Thornton Hall
Charlottesville, VA 22903

No. of Copies | Organization

1 Drexel University
Dept. of Materials Engineering
ATTN: H. C. Rogers
Philadelphia, PA 18104

1 SRI International
ATTN: D. Curran
333 Ravenswood Avenue
Menlo Park, CA 94025

1 SRI International
ATTN: R. Shockey
333 Ravenswood Avenue
Menlo Park, CA 94025

1 SRI International
ATTN: L. Seaman
333 Ravenswood Avenue
Menlo Park, CA 94025

USER EVALUATION SHEET/CHANGE OF ADDRESS

This Laboratory undertakes a continuing effort to improve the quality of the reports it publishes. Your comments/answers to the items/questions below will aid us in our efforts.

1. ARL Report Number ARL-TR-133 Date of Report May 1993

2. Date Report Received _____

3. Does this report satisfy a need? (Comment on purpose, related project, or other area of interest for which the report will be used.) _____

4. Specifically, how is the report being used? (Information source, design data, procedure, source of ideas, etc.) _____

5. Has the information in this report led to any quantitative savings as far as man-hours or dollars saved, operating costs avoided, or efficiencies achieved, etc? If so, please elaborate. _____

6. General Comments. What do you think should be changed to improve future reports? (Indicate changes to organization, technical content, format, etc.) _____

CURRENT ADDRESS

_____
Organization

_____
Name

_____
Street or P.O. Box No.

_____
City, State, Zip Code

7. If indicating a Change of Address or Address Correction, please provide the Current or Correct address above and the Old or Incorrect address below.

OLD ADDRESS

_____
Organization

_____
Name

_____
Street or P.O. Box No.

_____
City, State, Zip Code

(Remove this sheet, fold as indicated, tape closed, and mail.)
(DO NOT STAPLE)

DEPARTMENT OF THE ARMY

OFFICIAL BUSINESS

BUSINESS REPLY MAIL
FIRST CLASS PERMIT No 0001, APG, MD

Postage will be paid by addressee

Director
U.S. Army Research Laboratory
ATTN: AMSRL-OP-CI-B (Tech Lib)
Aberdeen Proving Ground, MD 21005-5066

NO POSTAGE
NECESSARY
IF MAILED
IN THE
UNITED STATES